Pergamon

Geochimica et Cosmochimica Acta, Vol. 62, No. 18, pp. 3161–3168, 1998

0016-7037/98 $19.00 + .00

PII S0016-7037(98)00216-6

UV laser ablation and *irm*-GCMS microanalysis of $^{18}O/^{16}O$ and $^{17}O/^{16}O$ with application to a calcium-aluminium-rich inclusion from the Allende meteorite

EDWARD D. YOUNG,[1,*] DAVID W. COUTTS,[2] and DANIEL KAPITAN[2]

[1]Department of Earth Sciences, University of Oxford, Oxford OX1 3PR, U.K.
[2]Department of Atomic and Laser Physics, Clarendon Laboratory, University of Oxford, Oxford OX1 3PU, U.K.

Abstract—Analyses of $^{18}O/^{16}O$ and $^{17}O/^{16}O$ in silicate and oxide minerals by UV laser ablation of $100 \times 80 \times 50$ μm sample pits combined with *irm*-GCMS yield precision and accuracy similar to that of conventional methods. This represents a 100-fold reduction in minimum size relative to other fluorination methods based on gas-source mass spectrometry and enables high-precision in-situ intracrystalline analysis of silicate minerals.

Analyses of almandine, forsterite, and schorl of known isotopic compositions indicate an analytical precision of ± 0.3‰ (1σ) in $\delta^{18}O$ and ± 0.4 in $\delta^{17}O$ with an accuracy of similar magnitude. Application to meteoritic samples is demonstrated by *in-situ* analysis of pyroxene and melilite from a type B CAI inclusion from the Allende meteorite. The CAI data adhere to the carbonaceous chondrite anhydrous mineral line defined by conventional macroscopic fluorination methods and demonstrate that non-mass dependent differences of 1‰ amu^{-1} are discernible. The unique combination of analytical and spatial resolution afforded by the new UV laser microprobe will allow high-precision mapping of the distribution of anomalous oxygen in minerals from calcium-aluminum-rich inclusions on a previously unattainable scale. *Copyright © 1998 Elsevier Science Ltd*

1. INTRODUCTION

Methods for microanalysis of oxygen isotope ratios in silicate minerals are being sought with vigor. Motivation for technique development comes in part from the vexing problem of the origin of anomalous oxygen isotope ratios in meteorites (e.g., Yurimoto et al., 1994; Leshin et al., 1997; Engrand et al., 1997). Secondary ion mass spectrometry (SIMS) has been used to obtain measurements with spatial resolution on the order of 20 μm or less. The cost of this high spatial resolution has been poor analytical precision compared with oxygen extraction by fluorination and gas-source isotope ratio mass spectrometry (FMS). SIMS affords precision on the order of ± 1–2‰ amu^{-1} (1σ) for the large majority of applications (e.g., Valley and Graham, 1996; Leshin et al., 1997; Lyon et al., 1998) while most FMS methods are assured of ± 0.2 amu^{-1} precision and in many cases $< \pm 0.1$‰ has been obtained (e.g., Valley et al., 1995). Sub-per mil precision is useful for distinguishing mass-dependent from nonmass dependent relations among ^{16}O, ^{17}O, and ^{18}O where the total range in $^{18}O/^{16}O$ is limited.

Wiechert and Hoefs (1995) and Rumble *et al*. (1997) have demonstrated that ultraviolet (UV) laser ablation in F_2 gas can be used to obtain in situ analyses of $^{18}O/^{16}O$ and $^{17}O/^{16}O$ with precision rivaling conventional FMS methods. These workers have shown that UV ablation is superior to infrared (IR) heating as a means for liberating oxygen because the material left behind is not thermally affected; partial melting in the annular zones surrounding pits limits the size of *in situ* analysis spots by IR heating to ≥ 1 mm (e.g., Young and Rumble, 1993).

In permitting *in situ* analysis, UV lasers have the potential to be used as oxygen isotope microprobes. Until now, however, UV laser ablation-fluorination has been limited to O_2 sample sizes greater than 1 μmol (approximately 0.1 mg of silicate) in part because the gas-source mass spectrometers used rely on viscous flow of sample gases.

We report here the development of a UV ablation-fluorination microprobe that extends the use of laser ablation for oxygen isotopic analysis to the nanomole level (approximately 1 μg of silicate) by preconcentrating oxygen from a fluorination vacuum extraction line for analysis by isotope-ratio-monitoring gas chromatography/mass spectrometry (*irm*-GCMS). Results show that O_2 extracted from ablation pits measuring approximately $80 \times 100 \times 50$ μm can be analyzed for $\delta^{18}O$ and $\delta^{17}O$ with precision of 0.3 and 0.4‰, respectively, and accuracy of at least ~0.3‰. Application to meteoritic samples is demonstrated by *in situ* analysis of pyroxene and melilite from a type B CAI inclusion from the Allende meteorite. The CAI data adhere to the carbonaceous chondrite anhydrous mineral line defined by conventional FMS (Clayton, 1993) and demonstrate that nonmass dependent differences of 1‰ amu^{-1} are discernible.

2. THE LASER ABLATION AND FLUORINATION PROCESSES

Laser ablation and chemical processing of the ablated products are just beginning to be understood despite intensive study, especially by workers engaged in development of thin-film deposition methods. Nevertheless, it is clear that the scale of ablation may profoundly influence results. Further refinements of laser-fluorination and indeed other laser-based microanalysis methods will benefit from identification of the factors that control the quality of results. We, therefore, include a synthesis of the physico-chemical processes that likely give rise to the release of oxygen by laser ablation and fluorination.

*Author to whom correspondence should be addressed (ed.young@earth.ox.ac.uk).

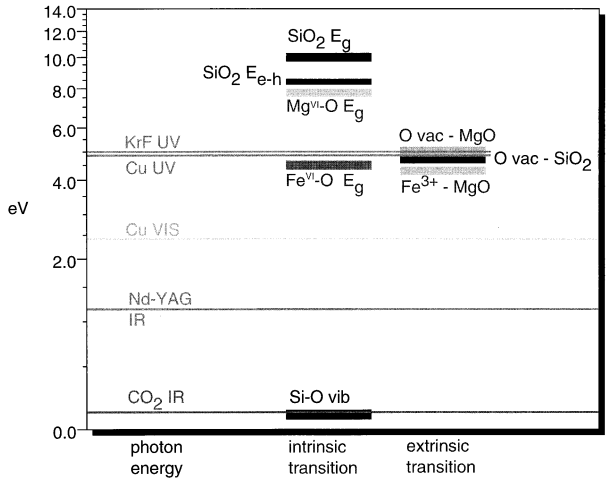

Fig. 1. Energy level diagram depicting the interactions between infrared (from a CO2 or Nd-YAG laser), visible (Cu vapor laser green), and ultraviolet (UV from a Cu vapor laser or a KrF laser) photons with silicate minerals. Illustrative laser light absorption mechanisms are shown for Si coordinated by four oxygens (SiO_2, black), Mg coordinated by eight oxygens (MgO, light grey), and Fe coordinated by eight oxygens (FeO, dark grey). IR light transfers energy to resonating vibrational modes. Those involving Si-O bonds are shown (Si-O vib). Multiphoton absorption allows UV light to couple intrinsically in silicates by promoting electrons across valence-conduction band gaps, represented here by the band-gap energies (E_g) in quartz and octahedrally coordinated Mg and Fe. Exciton formation effectively narrows the band gap, producing a lower transition energy (E_{e-h}) shown here for α quartz. Defects that enable extrinsic coupling between UV photons and electronic transitions include O vacancies in MgO and SiO_2 and charge transfer due to the presence of ferric iron impurities in MgO. Energy levels are from references cited in the text as well as from Bukowinski (1980) and Sherman (1991).

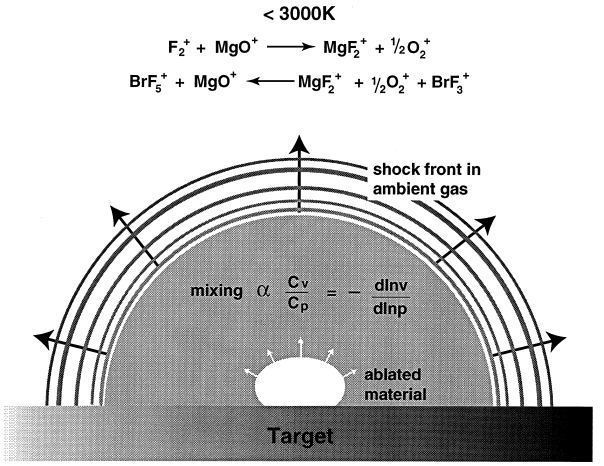

Fig. 2. Schematic illustration of a blast wave in a background gas induced by plasma during UV ablation of mineral material. The degree of mixing between ablation products exiting the plasma and ambient gas behind the shock front (grey zone) depends upon gas density and the ratio of isobaric (Cp) to isochoric (Cv) heat capacity in the reagent. Two possible reactions involving either ionized BrF_5 or ionized F_2 in the mixing zone behind the shocked and partially ionized fluorinating gas are shown. Fluorination of oxides is expected for the latter but not for the former below 3000 K.

2.1. Ablation

UV photons are absorbed by transitions in electron energy levels. Vibrational-electronic coupling occurs within $<10^{-15}$ sec leading to lattice vibrations and ultimately extreme *localized* heating of the medium. Duley (1996) estimates that photon-driven reactions dominate over thermally-driven reactions for times t less than $t' = \lambda^2/(4\kappa)$ where λ is the incident wavelength and κ is thermal diffusivity. For UV ($\lambda = 250$ nm) ablation of rock-forming minerals one obtains $t' = 2 \times 10^{-8}$ s. Apparently, a principal reason for the negligibly small heat affected zones surrounding UV ablation pits is that the pulse length of most commonly used UV sources is on the order of t', e.g., 3×10^{-8} s in the case of the frequency-doubled Cu vapor laser used in the present study.

Transitions responsible for absorption of UV photons include promotion of electrons across the bandgap, formation of excitons, and electron transitions within defect absorption centers. Bandgap energies of many geologically relevant minerals exceed the 4.9–6.4 eV of UV photons used in most experiments (Fig. 1) and so excitation by absorption of single photons is not possible. Excitons are localized electron-hole pairs bound to one another at lattice positions, in some cases on individual O ions (e.g., Zhang et al., 1994). They enhance the opportunity for intrinsic absorption by providing hydrogen-like energy levels below the bottom of the conduction band as a result of coulombic attraction between the electron and hole. Nevertheless, the energy required for exciton formation is comparable to the bandgap (Guizard et al., 1995) and multiphoton absorption is required for either exciton or bandgap transitions (Fig. 1).

Comparison of average photon densities (Poisson probability distributions) with atomic densities in silicate rock-forming minerals indicates that the probability of two-photon absorption relative to single-photon absorption is $\leq 10^{-7}$ for the power densities of 1×10^8 to 1×10^9 W cm^{-2} commonly used for mineral ablation. Irradiance must exceed 10^{15} W cm^{-2} for the probability of multiphoton interaction, and hence intrinsic absorption, to dominate.

The residence time of an electron in the conduction band, τ, is on the order of 150 fs (Guizard et al., 1995). From τ, the density of bonding electrons in silicate, and interband transition energies (e.g., 2×10^{23} electrons per cm^3 and 8.7 eV, respectively) it is evident that the 10^{15} W cm^{-2} required for dominance of multiphoton absorption is sufficient to promote nearly all bonding electrons to an excited state simultaneously. Bleaching (transparency to UV) is expected to occur as the UV absorption coefficient decreases and the saturated column of mineral becomes increasingly transparent. We suggest that the cracking and explosive ablation commonly observed at power densities near 10^{15} W cm^{-2} (see Luft et al., 1996 for examples) is explained in part as a consequence of bleaching. Bond scission and distortion by the laser at depths within the mineral below the bleached zone cause a buildup of gas pressure and mechanical stress. Explosive ablation involves particulate ejection and will not produce the molecules, atoms, and ions necessary for liberation of oxygen by chemical reaction with fluorine. Surface pressures at $>10^9$ W cm^{-2} rapidly increase beyond several hundred bar (Dreyfus, 1995) and will also cause ejection of macro-particles. For these reasons we expect that

power densities sufficient for intrinsic-dominated absorption and bleaching will be of little use in laser ablation fluorination.

Because intrinsic absorption is limited, UV ablation of silicates to form reactants for fluorination must rely on absorption by defects. Typical defect transitions, including charge transfer accommodated by Fe^{3+} impurity and charged or neutral oxygen vacancies, range from 6 eV to 4 eV (Fig. 1) and are accessible by absorption of single UV photons at moderate power densities. Experiments with quartz suggest that two-photon absorption during UV exposure creates excitons that decay non-radiatively into oxygen vacancies (Joosen et al., 1992; Itoh et al., 1994; Duley, 1996). In this way ablation might be initiated in the absence of *preexisting* impurities and defects as the number of vacancies increases.

The ablation process at moderate power density is envisaged as follows: UV irradiation augments an existing defect density with exciton-induced vacancies by infrequent multiphoton excitation. The number of defects increases with continued exposure until a threshold defect density is attained. Beyond this threshold, single-photon extrinsic absorption is sufficient for ablation. Such a process is consistent with experimental evidence in wide-bandgap materials for an induction period of laser irradiation before ablation can begin (accumulation of a minimum defect density) and lack of fluence-dependent absorption characteristics (indicating single-photon domination of absorption, Lowndes et al., 1993).

2.2. Fluorination

Fluorination by IR laser heating is accomplished by reaction between fluorinating gas (F_2 or BrF_5) and molten mineral. In the case of UV laser ablation, fluorination occurs in or adjacent a plume of hot plasma that forms above the target mineral while the laser pulse is active. Unpublished experiments conducted as part of the present study demonstrate that fluorination of UV ablation products is more efficacious in F_2 gas than in BrF_5. Reasons for this disparate behavior are suggested below.

The body of knowledge on laser-induced plasmas indicates that interaction between ambient fluorinating gas and silicate plasma plumes should be sensitive to the dynamics of the plume and surrounding background gas. There is also evidence that thermodynamic forces may play a role despite the extreme conditions and short time scales involved.

Immediately above the ablation site temperatures reach several thousands of degrees K as indicated by the incandescence in the center of the plume and theoretical and experimental measurements of laser ablation-induced plasma plumes above oxide targets (e.g., Le et al., 1996). Rapid acceleration of atoms and molecules from the ablation pit compresses the background fluorinating gas. A Taylor-Sedov blast wave is triggered that propagates through the fluorinating medium (Fig. 2). Theory predicts that the strength and stability of the blast wave will depend on laser pulse energy, total background gas pressure, and properties of the background gas. Theoretical dependence of shock intensity on background gas properties has been confirmed experimentally by Kapitan et al. (1998) using a ballistic pendulum.

Transient temperatures in the stable blast wavefront may be as high as 30000 K (Le et al., 1996). Ionization of the fluorinating gas in the wavefront is therefore likely (Callies et al., 1995). Fluorination is favored where separation between the blast front in the ambient gas and the ablation plasma plume is incomplete. Under these conditions excited ablation products (molecular and atomic neutrals and ions) diffuse into the heated and partially ionized rarefied background gas left behind in the wake of the blast wave. The degree of separation correlates with the intensity of the shock wave. Shock intensity and degree of separation are quantified by the wavefront pressure P_i in ambient gas phase i. Wavefront pressure in turn varies with ambient gas density ρ_i and the adiabatic constant γ_i (the ratio of isobaric to isochoric heat capacity) according to the expression (Sedov, 1993; Guggenheim, 1967)

$$P_i \simeq \frac{2}{\gamma_i + 1} \rho_i v_i^2 \tag{1}$$

where v_i is the wavefront velocity. Using the analysis of shock front propagation by Callies et al. (1995) it can be shown that the velocity of a shock front in BrF_5 will be approximately 0.74 that in F_2 (based on different gas densities at equivalent pressures and laser pulse energies). The ratio of front pressures is, therefore,

$$\frac{P_{F_2}}{P_{BrF_5}} = 0.444 \frac{\gamma_{BrF_5} + 1}{\gamma_{F_2} + 1}. \tag{2}$$

Adiabatic constants generally vary from 1 to 1.7 and can be estimated using the relation $\gamma = (1 + 2/f)$ where f is the internal degrees of freedom associated with the gas molecule. One obtains $\gamma_{F_2} \sim 1.3$ and $\gamma_{BrF_5} \sim 1.1$ with this relation and the pressure in the blast wavefront in BrF_5 will be 2–3 times that in F_2. As the front moves faster in F_2 but the front pressure is greater in BrF_5, the shock wave attending laser ablation sweeps BrF_5 from the plasma environs more effectively than in the case of F_2, inhibiting the effectiveness of BrF_5 as a fluorinating agent.

Rumble et al. (1997) showed that although UV ablation in BrF_5 yields reasonable isotopic measurements, precision and accuracy are improved using F_2 gas. In this study, hundreds of ablation-fluorination experiments were carried out using BrF_5 with limited success (the data are too numerous to report in detail in this communication). In general, oxygen isotopic ratios obtained by ablation in BrF_5 were substantially more erratic than those observed by Rumble et al. (1997), with deviations from expected values commonly as high as ± 5 per mil. The degradation in accuracy and precision associated with ablation in BrF_5 at the millimeter scale (Rumble et al., 1997) is exaggerated at the 100 μm scale of the present experiments. Isotope ratios of O_2 liberated by ablation in BrF_5 exhibit a linear relation with sample size in some data sets. In other instances no systematic variability is evident. In contrast, under identical conditions, ablation in F_2 yields consistent oxygen isotope ratios, indicating complete fluorination of ablated silicate. We suggest that the efficacious fluorination of ablated material by F_2 gas and the apparent incomplete and inconsistent fluorination by BrF_5 vapor may be explained in part by the different physical properties of the two fluorinating agents and the effects of these differences on the dynamics of the shock wave that forms above the ablation plasma plume.

In addition to dynamical considerations, it is possible to examine the relative merits of F_2 and BrF_5 in terms of thermo-

Table 1. Analyses of almandine garnet, Smithsonian Institution specimen 107144. Expected values are 6.0‰ and 3.1‰ for $\delta^{18}O$ and $\delta^{17}O$, respectively.

$\delta^{18}O^1_{SMOW}$	$\delta^{17}O^1_{SMOW}$	$\Delta^{17}O^2$	Yield (nmol)[3]
5.7	3.2	0.3	19
5.4	3.0	0.2	16
6.2	3.2	0.0	17
6.0	2.8	−0.3	17
6.2	3.1	−0.1	16
6.6	3.1	−0.3	14
5.7	2.7	−0.2	13
6.2	3.5	0.3	17
6.4	2.9	−0.4	14
6.5	4.3	1.0	14
6.0	2.3	−0.8	12
6.2	2.8	−0.4	16
6.3	3.0	−0.2	12
5.6	3.4	0.5	9
5.9	2.8	−0.2	12
6.5	3.2	−0.1	6
5.9	3.0	0.0	12
6.1	3.1	0.0	mean
±0.3	±0.4	±0.4	1σ

[1] Analyses corrected for blank using peak areas in V · s.
[2] Excess ^{17}O calculated from measured values as $\delta^{17}O - 0.514\ \delta^{18}O$ as prescribed by the tangent to the mass fractionation curve.
[3] Determined by $m/z = 32$ peak areas based on 0.6 or 1.8 V s per nmol as appropriate.

Table 2. Analyses of schorl, Smithsonian Institution specimen R11871-1. Expected values are 9.2‰ and 4.7‰ for $\delta^{18}O$ and $\delta^{17}O$, respectively.

$\delta^{18}O^1_{SMOW}$	$\delta^{17}O^1_{SMOW}$	$\Delta^{17}O^2$	Yield (nmol)[3]
8.9	4.4	−0.2	13
8.8	4.3	−0.2	11
8.2	4.1	−0.2	12
8.6	4.2	−0.2	mean
±0.4	±0.2		1σ

[1] Analyses corrected for blank using peak areas in V · s.
[2] Excess ^{17}O calculated from measured values as $\delta^{17}O - 0.514\ \delta^{18}O$.
[3] Determined by $m/z = 32$ peak areas based on 0.6 or 1.8 V s per nmol as appropriate.

Table 3. Analyses of forsterite olivine, Smithsonian Institution specimen 107144. Expected values are 5.2‰ and 2.7‰ for $\delta^{18}O$ and $\delta^{17}O$, respectively.

$\delta^{18}O^1_{SMOW}$	$\delta^{17}O^1_{SMOW}$	$\Delta^{17}O^2$	Yield (nmol)[3]
5.5	2.8	0.0	13
5.8	2.2	−0.8	15
5.3	2.8	0.1	17
5.7	3.7	0.8	16
6.0	4.2	1.1	14
5.5	2.6	−0.2	16
5.6	3.1	0.2	mean
±0.3	±0.7	±0.7	1σ

[1] Analyses corrected for blank using peak areas in V · s.
[2] Excess ^{17}O calculated from measured values as $\delta^{17}O - 0.514\ \delta^{18}O$.
[3] Determined by $m/z = 32$ peak areas based on 0.6 or 1.8 V s per nmol as appropriate.

Table 4. UV ablation and *irm*-GCMS analyses of a type B CAI from the Allende meteorite.

$\delta^{18}O^1_{SMOW}$	$\delta^{17}O^1_{SMOW}$	Minerals	Yield (nmol)[2]
−4.1	−8.2	melilite ≫ spinel	10
−7.4	−11.1	melilite ≫ spinel	10
−5.4	−9.0	melilite ≫ spinel	15
−3.8	−8.8	melilite ≫ spinel	–[3]
−26.8	−29.0	pyroxene > spinel	10
−28.1	−30.9	pyroxene > spinel	11

[1] Analyses corrected for blank using peak areas in V · s.
[2] Determined by $m/z = 32$ peak areas based on 0.6 or 1.8 V s per nmol as appropriate.
[3] Not recorded for this analysis, but similar to others.

dynamics. Dreyfus (1995) points out that the time scale of forming oxidation products by ablation of Cu in an O_2 atmosphere is very much longer (up to 300 μs) than the transit time of reactant ablation species (<5 μs) at positions above the target, implying that reaction takes place after reactants have been slowed by multiple collisions. Thermodynamics can be used to predict the relative stabilities of species under such conditions.

Among thirty equilibria representing possible reactions between ablation products and reagent in the systems $BrF_3 + F + O + Mg + e$ and $F + Mg + O + e$ (e representing electrons to account for ionic species), all but three strongly favor liberation of oxygen at the pressures and temperatures considered (thermochemical data from JANAF tables, Chase et al., 1985). Of those that do not favor fluorination, the reactions

$$F_2^0 + Mg^0 + 2O^0 \rightleftharpoons MgF_2^0 + O_2^0 \quad (3)$$

and

$$2F^0 + Mg^0 + 2O^0 \rightleftharpoons MgF_2^0 + O_2^0 \quad (4)$$

proceed from right to left above approximately 5000 K and are of little relevance outside of the plasma plume itself. The third

$$BrF_5^+ + MgO^+ \rightleftharpoons MgF_2^+ + \tfrac{1}{2}\,O_2^+ + BrF_3^+ \quad (5)$$

proceeds from right to left below approximately 3000 K (subplume temperatures). As a consequence, bromine pentafluoride may not fluorinate some molecular ions outside of the plasma plume regardless of the degree of intermingling.

3. EXPERIMENTAL METHODS

3.1. Ultraviolet Laser Ablation

The ultraviolet laser beam (255 nm) used for ablation is generated by frequency doubling the green (510.6 nm) output from an Oxford Lasers LS-10 copper-vapor laser (CVL). The CVL is fitted with a custom on-axis resonator that preserves the far-field characteristics of the incident green beam in the UV. Frequency doubling is accomplished by line focusing through a BBO crystal as described by Coutts and Brown (1995). Spatial filtering yields 8 Watts of the fundamental green and a maximum UV power output of 600 mW. Experiments reported here were performed with 450–500 mW of UV delivered at a pulse repetition rate of 4 kHz, yielding a pulse energy of 0.1 mJ. It is expected that this low pulse energy minimizes the expulsion of μm-sized particles (i.e., particles too large for fluorination). Pulse width is 30 ns (FWHH). Average pulse fluence of 30 ± 5 J cm^{-2} is obtained by focusing the collimated beam to a spot measuring 25 μm in diameter.

A chopper wheel is used to modulate the 4 kHz laser to 10 or 20 Hz bursts. This additional modulation does not alter the pulse characteristics of the laser (bursts consist of 30 ns pulses at 4 kHz) and has no measurable effect on isotope ratios but allows improved control over the depth of ablation. Pits were made by slowly rastering the 25 μm spot.

3.2. Fluorination

The vacuum extraction line used in the present experiments is composed of 316L stainless steel tubing and low-dead volume fittings and valves. It is evacuated by a corrosive-grade turbomolecular pump, a backing rotary pump, and a low-vacuum rough pump for sample changing. The volume of the sample chamber is approximately 13 cm^3. A complete diagram of the extraction line is presented by Young et al. (1998).

Fluorine is generated using solid $K_2NiF_6 \cdot KF$ as described by Asprey (1976). The F_2 generator is a commercial device (Oxford Lasers) consisting of a temperature-controlled cylindrical container filled with 60 cm^3 of $K_2NiF_6 \cdot KF$ powder. Fluorine pressures in the sample chamber varied from 5 to 15 mbar for the experiments reported here. Oxygen blank from the generator is below detection ($\ll$1 nmol) on our system. Excess F_2 was passivated using a high-conductance KBr trap.

3.3. Pre-concentration of O_2 and *irm*-GCMS

Oxygen gas was the analyte for all experiments. Young et al. (1998) present results of tests showing that nanomole quantities of O_2 gas can be transferred with isotope fidelity from the vacuum line to the *irm*-GCMS instrumentation. The most important component of the O_2-handling system is the pre-concentration device comprising the interface between vacuum and He carrier gas. Carrier-gas flows in this device are precisely controlled by fixed lengths of fused silica tubing to minimize background (blank) oxygen that comes from leaky gas chromatography seals (Young et al., 1998).

The *irm*-GCMS system is composed of a Finnigan MAT 252 gas-ratio mass spectrometer, a Shimadzu GC-R1A gas chromatograph (GC), and a Finnigan MAT GC-MS interface based on technology described by Merritt et al. (1994). Oxygen gas is passed through a 5A molecular sieve PLOT column for purification prior to admission to the GC-MS interface. The column has a 0.53 mm internal diameter and is 10 m in length. Operating temperature of the GC was a constant 50°C for all experiments. Commercial oxygen/water traps and a molecular sieve trap cooled to liquid N_2 temperature purge the He carrier gas of detectable oxygen.

Oxygen from air was the primary calibration standard for this study. All isotope ratios are reported in the δ notation where δ refers to the per mil (per thousandth) deviation in $^{18}O/^{16}O$ or $^{17}O/^{16}O$ of sample relative to standard mean ocean water (SMOW). A $\delta^{18}O$ value of 23.3‰ relative to SMOW was obtained for a sample of local air at the time the data of this study were collected. For comparison, Craig (1972) reports a mean air $\delta^{18}O$ value of 23.5‰ relative to SMOW.

Corrections were made for system blank as described by Young et al. (1998). Blanks were typically on the order of 1–2 nmol with $\delta^{18}O$ and $\delta^{17}O$ values of approximately 11.0 and 5.7‰, respectively. Measurements of blank were made before and after data collection to ensure consistency.

4. RESULTS

4.1. Standardization

Tables 1, 2, and 3 summarize results of in situ microanalysis of three silicate minerals for which isotope ratios had been determined previously. These minerals were chosen as reference samples because they have been shown to be homogeneous on the millimeter scale using UV and IR laser methods (Rumble et al., 1997).

Data for the reference minerals indicate a precision of ±0.3‰ for $\delta^{18}O$ and ±0.4‰ for $\delta^{17}O$. Accuracy is between 0.1 and 0.6‰ (Fig. 3) with a mean of 0.3‰. A more precise figure for accuracy is not possible because accepted values vary as a function of method of analysis (see Rumble et al., 1997 for discussion of the values assigned to these minerals).

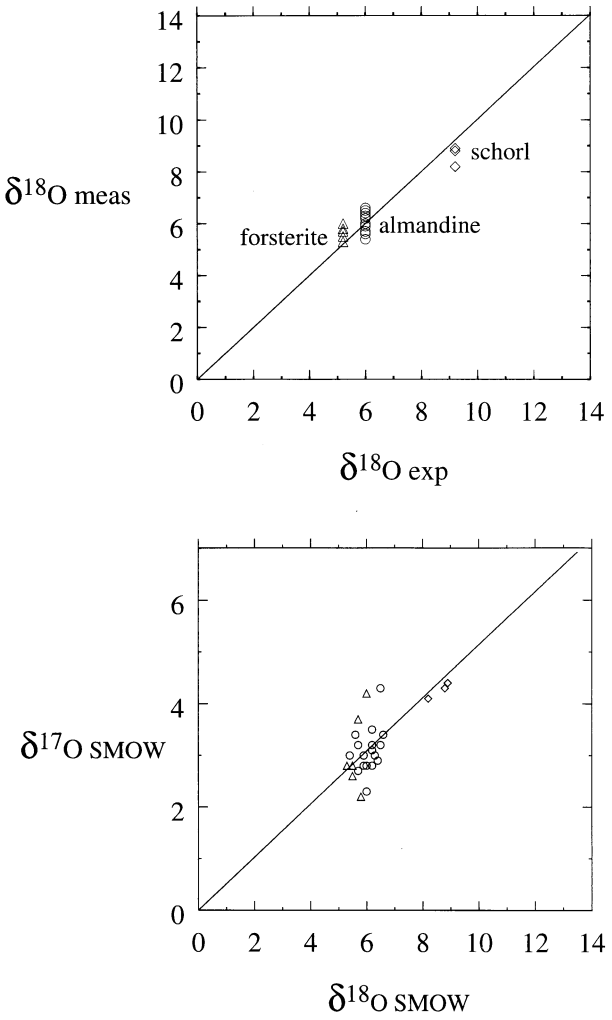

Fig. 3. Plot of measured $\delta^{18}O$ values for reference samples against expected $\delta^{18}O$ (upper panel) and measured $\delta^{17}O$ (lower panel). Line in the upper panel has a slope of 1. The line in the lower panel is the terrestrial mass fractionation curve.

Gaseous H_2O, N_2, NF_3, and CF_4 are known to interfere with mass spectrometer detection of the O_2 isotopomers $^{17}O^{16}O$ and $^{18}O^{16}O$ to varying degrees and can cause erroneous relationships between $^{17}O/^{16}O$ and $^{18}O/^{16}O$. Monitoring of mass-to-charge values of 18, 28, 52, and 69 using the most sensitive amplified collector shows no indication of these gases coeluting with O_2, and the data adhere to the average terrestrial mass fractionation curve (Fig. 3) to within 0.4‰. Conventional FMS methods require purification of O_2 by freezing to molecular sieve at −196°C followed by desorption at −130°C (e.g., Clayton and Mayeda, 1983). Desorption of nanomole quantities of O_2 gas from molecular sieve substrates at low temperatures causes isotope fractionation, and it is emphasized that agreement between measured values and the average terrestrial curve has been achieved without the use of molecular sieve traps.

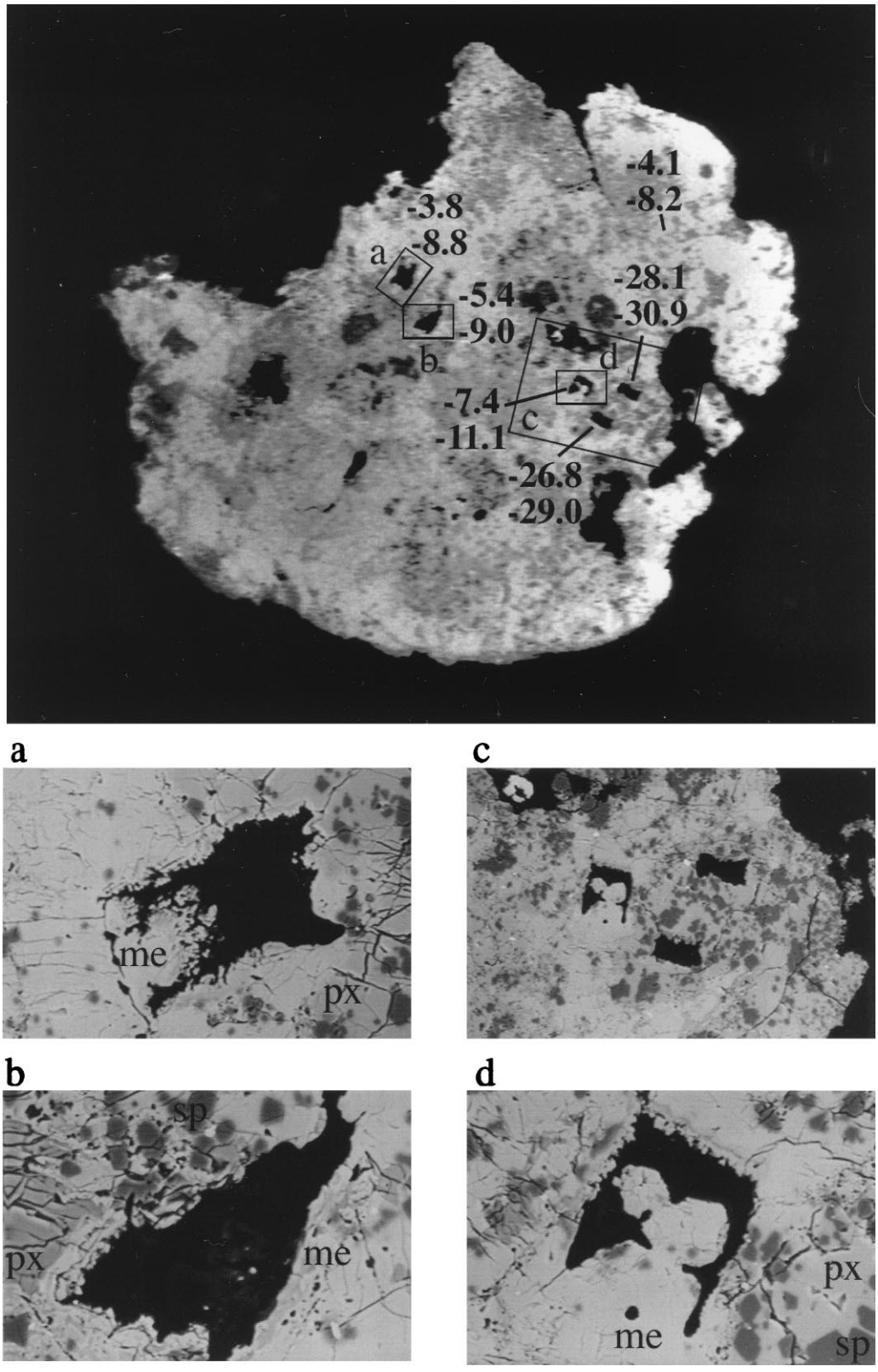

Fig. 4. Backscattered electron images of a section of the type B CAI from the Allende meteorite analyzed in this study. The section (30 μm in thickness) was made after UV ablation and shows the spatial relationships between the bottoms of the laser pits and the minerals analyzed. Long dimensions of the laser pits are 100 μm in each image. Average depths of pits are estimated to have been 50 μm but their bottoms were not flat, causing them to be represented by irregular shaped holes (black) in this section. The top panel shows the entire inclusion. Lower panels a, b, c, and d (indexed to the top panel) show blowups of the regions surrounding the laser pits. Light grey is melilite (me), medium grey is pyroxene (px), and dark grey is spinel (sp). Scale bars are 100 μm. Pits are labelled with measured $\delta^{18}O$ (upper) and $\delta^{17}O$ (lower) relative to SMOW. Note the qualitative correlation between the presence of spinel and excess ^{16}O in melilite analyses (compare a with b and d). The pit corresponding to the analysis in the upper right quadrant was polished away.

Gas-chromatographic methods, therefore, constitute an important advance for measurement of $^{17}O/^{16}O$ in nanomole samples of oxygen liberated by fluorination by allowing purification without isotope fractionation.

Five of the analyses exhibit anomalously large deviations from mass fractionation (approaching ±1‰). These are likely the result of moisture that is present for the first several hours that He is flowing through the instrument. We find that the problem of large excursions in $\delta^{17}O$ is avoided by heating the culpable valve to remove adsorbed water upon start up.

4.2. Allende CAI

Calcium-aluminum-rich inclusions from the Allende meteorite possess isotopically anomalous oxygen (Clayton et al., 1973). The array of Allende CAI data define a slope of nearly 1 (average slope of 0.92, Clayton et al., 1977) on a plot of $\delta^{17}O$ against $\delta^{18}O$, indicating nonmass dependent mechanisms for oxygen accumulation. The slope near 1 contrasts with the mass-fractionation slope of ~0.52 exhibited collectively by terrestrial materials. Previous studies have sought to constrain the origin of the anomalous oxygen in different components of Allende by searching for either mass-dependent or non-mass dependent intrainclusion or intracrystalline heterogeneity (e.g., Saxton et al., 1995; Weinbruch et al., 1993). Until now the only method available for microscopic sampling of $^{18}O/^{16}O$ and $^{17}O/^{16}O$ has been secondary ion mass spectrometry (SIMS). SIMS studies have suffered from inherent imprecision that aliases the distinction between mass-dependent and nonmass dependent trends unless variations are on the order of 5‰ or more, and it is not known to what spatial scale a strictly nonmass dependent relation between $\delta^{17}O$ and $\delta^{18}O$ persists in CAIs. As a consequence, while it is known that individual mineral grains from at least one CAI inclusion are homogeneous in $\delta^{18}O$ to ±5.0‰ (Yurimoto et al., 1994), it is not known whether or not intracrystalline heterogeneity on the order of 1‰ exists, and if so, whether that heterogeneity defines a three-isotope slope of 1, 0.52, or some other value. UV fluorination combined with *irm*-GCMS offers the ability to reveal deviations from non mass dependence on the order of 0.8‰ (i.e., 2σ) with high spatial resolution (approximately 100 μm).

A type B calcium-aluminum-rich inclusion from the Allende meteorite (sampled from USNM specimen 3576) was analyzed using UV ablation in F_2 and *irm*-GCMS of liberated O_2 as a test of the potential of this new method. The inclusion is composed principally of melilite, spinel, and pyroxene (Al and Ti-rich) with minor perovskite. Preliminary results for a single grain of pyroxene and several grains of melilite are given in Table 4, Fig. 4, and Fig. 5. Effort was made to analyze melilite adjacent pyroxene. Fine-grained spinel that is pervasive in regions surrounding pyroxenes in the inclusion could not be avoided with this sampling strategy and are included to varying degrees in each of the analyses (Fig. 4).

CAI in situ laser samples consisting of pyroxene > spinel and melilite ≫ spinel yield $\delta^{18}O$ and $\delta^{17}O$ values along a line that is statistically indistinguishable from the carbonaceous chondrite anhydrous mineral line (CCAM) as defined by FMS of Allende mineral separates (e.g., Clayton et al., 1977, Fig. 4). The relative $\delta^{18}O$ values of pyroxene and melilite are consistent with the mineral-separate data of Clayton et al. (1977) and show that the nonmass dependent relation between $\delta^{18}O$ and $\delta^{17}O$ in the CAI is preserved at the 100 μm scale (Fig. 4).

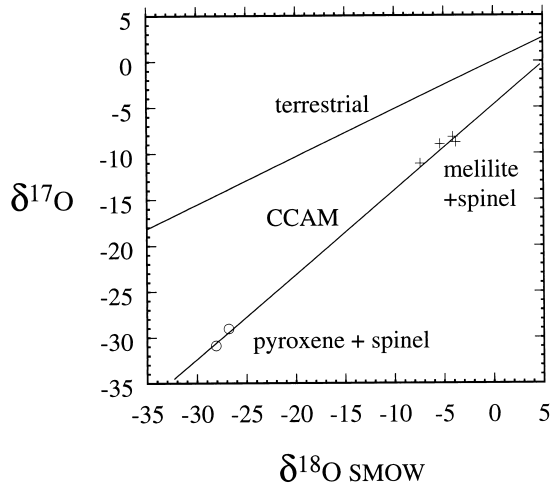

Fig. 5. Plot of data obtained by UV ablation, fluorination, and *irm*-GCMS for the CAI pictured in Figure 4. Circles represent pyroxene > spinel analyses, crosses represent melilite ≫ spinel analyses. The carbonaceous chondrite anhydrous mineral best-fit line (CCAM): $\delta^{17}O = 0.92(\pm 0.01\ 1\sigma)\delta^{18}O - 4.8(\pm 0.003\ 1\sigma)$ (linear regression of data for Allende presented by Clayton *et al*., 1977) is statistically indistinguishable from the best-fit line defined by these data: $\delta^{17}O = 0.93(\pm 0.05\ 1\sigma)\delta^{18}O - 4.5(\pm 0.03\ 1\sigma)$. The terrestrial mass fractionation curve is shown for reference.

Adherence of the CAI data to the CCAM is a powerful test of the new analytical method. Fractionation incurred as a result of UV ablation, fluorination, or gas handling would be mass dependent and manifested as deviations from the CCAM line with a slope of approximately 1/2. Numerical experiments with the data show that mass fractionation on the order of 2σ per amu would be easily discerned on a three-isotope plot.

The data define nonmass dependent variability that would not be resolvable by SIMS (Fig. 5). The degree of ^{16}O enrichment in analyses consisting of melilite ≫ spinel is clearly controlled by the amount of spinel (compare Fig. 4a and 4b). Thus these data define a mixing line between melilite and spinel. Nevertheless, they establish that neither the melilite nor the spinel deviates from the CCAM line due to mass fractionation at this spatial resolution. More data collected with UV fluorination and *irm*-GCMS will be required to search for correlations between $\delta^{18}O$, $\delta^{17}O$, and position in CAIs.

5. CONCLUSIONS

UV laser ablation in a fluorinating atmosphere for the purpose of oxygen isotope ratio analysis relies on laser coupling with defects in the mineral structure. Fluorination is complicated by dynamical interaction between the plasma plume above the ablation site and the ambient reagent gas. In combination these factors suggest the possibility that optimum conditions for UV laser fluorination may vary with scale and UV source.

Data presented here demonstrate that *irm*-GCMS can be combined with UV laser ablation in F_2 gas to obtain precise and

accurate $\delta^{18}O$ and $\delta^{17}O$ values for microgram (nanomole O_2) quantities of silicate minerals. Fluorine gas, not bromine pentafluoride, must be used to obtain useful data by UV laser ablation at the microgram sample level.

UV ablation in F_2 combined with *irm*-GCMS analysis of the liberated O_2 allows examination of the origin of anomalous oxygen in CAIs with a new level of scrutiny. Preliminary data show that a single type B CAI from the Allende meteorite shows no signs of mass dependent variations in $^{17}O/^{16}O$ and $^{18}O/^{16}O$ with a spatial resolution of 100 μm and an analytical resolution of approximately 0.8‰.

Acknowledgements—The authors are indebted to Dr. Douglas Rumble III, Professor Colin Webb, Dr. Michael Palin, Dr. Marilyn Fogel, Dr. Thomas Hoering (deceased), Dr. Uwe Weichert, Dr. Richard Ash, and Dr. Sara Russell for advice during the course of this study. Dr. Anthony J. Andrews was instrumental in designing and constructing the ultraviolet laser system for this research. Margaret Ricci kindly contributed software enabling us to analyze oxygen by *irm*-GCMS more conveniently. Alison Jones and Nicholas Gardner aided in collection of data. Financial support was provided by a grant from the U.K. Natural Environment Research Council (E.D.Y.) and by Oxford Lasers.

REFERENCES

Asprey L. B. (1976) The preparation of very pure F_2 gas. *J. Fluorine Chem.* **7,** 359–361.

Bukowinski M.S.T. (1980) Effect of pressure on bonding in MgO. *J. Geophys. Res. B* **85,** 285–292.

Callies G., Berger P., and Hugel H. (1995). Time-resolved observation of gas-dynamic discontinuities arising during excimer laser ablation and their interpretation. *J. Phys. D: App. Phys.* **28,** 794–806.

Chase M. W. Jr., Davies C. A., Downey J. R. Jr., Frurip D.J., and McDonald R.A. (1985) JANAF thermochemical tables third edition. *J. Phys. Chem. Ref. Data Suppl. No. 1* **14**.

Clayton R. N. (1993) Oxygen isotopes in meteorites. *Ann. Rev. Earth Planet. Sci.* **21,** 115–149.

Clayton R. N. and Mayeda T. K. (1983) Oxygen isotopes in eucrites, shergottites, nakhlites, and chassignites. *Earth Planet. Sci. Lett.* **62,** 1–6.

Clayton R. N., Grossman L., and Mayeda T. K. (1973) A component of primitive nuclear composition in carbonaceous meteorites. *Science* **182,** 485–488.

Clayton R. N., Onuma N., Grossman L., and Mayeda T. K. (1977) Distribution of the pre-solar component in Allende and other carbonaceous chondrites. *Geochim. Cosmochim. Acta* **34,** 209–224.

Coutts D. W. and Brown D. J. W. (1995) Production of high average power UV by second harmonic and sum-frequency generation from copper-vapor lasers. *IEEE J. Quant. Elect.* **1,** 768–778.

Craig H. (1972) Atmospheric oxygen: isotopic composition and solubility fractionation. *Science* **175,** 54–55.

Dreyfus R. W. (1995) Why are high-Tc superconductors, HTSC, deposited by 248 nm lasers at 400 MW/cm^2? *Appl. Surface Sci.* **86,** 29–34.

Duley W. W. (1996) *UV Lasers: Effects and Applications in Materials Science*. Cambridge Univ. Press.

Engrand C., McKeegan K. D., and Leshin L. A. (1997) In situ analysis of the oxygen isotopic composition of individual minerals in Antarctic micrometeroties. *Meteoritics Planet. Sci.* **32,** A39–A40.

Guggenheim E. A. (1967) *Thermodynamics: An Advanced Treatment for Chemists and Physicists*. North-Holland Physics Pub.

Guizard S., Martin P., Daguzan P., Petite G., Audebert P., Geindre J. P., Santos A. D., and Antonnetti A. (1995) Contrasted behaviour of an electron gas in MgO, Al_2O_3 and SiO_2. *Europhys. Lett.* **29,** 401–406.

Itoh N., Shimizu-Iwayama T., and Fujita T. (1994) Excitons in crystalline and amorphous SiO_2: Formation, relaxation and conversion to Frenkel pairs. *J. Non-Crystall. Solids* **179,** 194–201.

Joosen W., Guizard S., Martin P., Petite G., and Agostini P. (1992) Femtosecond multiphoton generation of the self-trapped exciton in α-SiO_2. *Appl. Phys. Lett.* **61,** 2260–2262.

Kapitan D., Coutts D. W., and Webb C. E. (1998) Gasdynamical studies of laser generated plasmas using a ballistic pendulum. European Conference on Lasers and Electro-Optics (CLEO/Europe), *Technical Digest*, CMF8.

Le H. C., Vuillon J., Zeitoun D., Marine W., Sentis M., and Dreyfus R. W. (1996) 2D modeling of laser-induced plume expansion near the plasma ignition threshold. *Appl. Surf. Sci.* **96–98,** 76–91.

Leshin L. A., Rubin A. E., and McKeegan K. D. (1997) The oxygen isotopic composition of olivine and pyroxene from CI chondrites. *Geochim. Cosmochim. Acta* **61,** 835–846.

Lowndes D. H., DeSilva M., Godbole M. J., Pedraza A. J., and Geohegan D. B. (1993) Ablation, melting, and smoothing of polycrystalline alumina by pulsed excimer laser radiation. In *Laser Ablation in Materials Processing: Fundamentals and Applications* (ed. B. Braren et al.); *Mat. Res. Soc. Symp. Proc.* **285,** 191–214.

Luft A., Franz U., Emsermann A., and Kaspar J. (1996) A study of thermal and mechanical effects on materials induced by pulsed laser drilling. *Appl. Phys. A* **63,** 93–101.

Lyon I. C., Saxton J. M., and Cornah S. J. (1998) Isotope fractionation during secondary ioniszation mass spectrometry: Crystallographic orientation effects in magnetite. *In. J. Mass Spect. Ion Proc.* **172,** 115–122.

Merritt D. A., Brand W. A., and Hayes J. M. (1994) Isotope-ratio monitoring gas chromatography-mass spectrometry: Methods for isotopic calibration. *Org. Geochem.* **21,** 573–583.

Rumble D. III, Farquhar J., Young E. D., and Christensen C. P. (1997) In situ oxygen isotope analysis with an excimer laser using F_2 and BrF_5 reagents and O_2 gas as analyte. *Geochim. Cosmochim. Acta* **61,** 4229–4234.

Saxton J. M., Lyon I. C., and Turner G. (1994) Minor elements and oxygen isotopes in forsterite grains in Julesburg and Allende. *Meteoritics* **29,** 528–529.

Sedov L. I. (1993) *Similarity and Dimensional Methods in Mechanics*. CRC Press.

Sherman D. M. (1991) The high-pressure electronic structure of magnesiowustite (Mg,Fe)O: Applications to the physics and chemistry of the lower mantle. *J. Geophys. Res. B* **96,** 14299–14312.

Valley J. W. and Graham C. M. (1996) Ion microprobe analysis of oxygen isotope ratios in quartz from Skye granite: Healed microcracks, fluid flow, and hydrothermal exchange. *Contrib. Mineral. Petrol.* **124,** 225–234.

Valley J. W., Kitchen N., Kohn M. J., Niendorf C. R., and Spicuzza M. J. (1995) UWG-2, a garnet standard for oxygen isotope ratios: Strategies for high precision and accuracy with laser heating. *Geochim. Cosmochim. Acta* **59,** 5223–5231.

Weichert U. and Hoefs J. (1995) An excimer laser-based micro analytical preparation technique for in-situ oxygen isotope analysis of silicate and oxide minerals. *Geochim. Cosmochim. Acta* **59,** 4093–4101.

Weinbruch S., Zinner E. K., El Goresy A., Steel I. M., and Palme H. (1993) Oxygen isotope composition of individual olivine grains from the Allende meteorite. *Geochim. Cosmochim. Acta* **57,** 2649–2661.

Young Edward D. and Rumble D. III (1993) The origin of correlated variations in in-situ $^{18}O/^{16}O$ and elemental concentrations in metamorphic garnet from southeastern Vermont, USA. *Geochim. Cosmochim. Acta* **57,** 2585–2597.

Young Edward D., Fogel, M. L., Rumble D. III, and Hoering T. C. (1998) Isotope-ratio-monitoring of O_2 for microanalysis of $^{18}O/^{16}O$ and $^{17}O/^{16}O$ in geological materials. *Geochim. Cosmochim. Acta* **62,** 3087–3094 (this issue).

Yurimoto H., Nagasawa H., Mori Y., and Matsubaya O. (1994) Microdistribution of oxygen isotopes in a refractory inclusion from the Allende meteorite. *Earth Planet. Sci. Lett.* **128,** 47–53.

Zhang X., Ong C. K., and Stoneham A. M. (1994) Stability of a self-trapping hole in α-quartz. *J. Phys. Condens. Matter* **6,** 5647–5656.